

# Quantitative Photoemission Predictions of Semiconducting Photocathodes from Many-Body *Ab Initio* Theory

Richard Schier,<sup>1, 2, \*</sup> Chen Wang,<sup>3, 4</sup> Jonas Dube,<sup>3, 5</sup> Julius Kühn,<sup>3</sup>  
Alice Galdi,<sup>3, 6</sup> Thorsten Kamps,<sup>3, 5</sup> and Caterina Cocchi<sup>1, 2, †</sup>

<sup>1</sup>*Carl von Ossietzky Universität Oldenburg, Institute of Physics, 26129 Oldenburg, Germany*

<sup>2</sup>*Friedrich-Schiller Universität Jena, Institute for Condensed Matter Theory and Optics, 07743 Jena, Germany*

<sup>3</sup>*Helmholtz-Zentrum Berlin, 12489 Berlin, Germany*

<sup>4</sup>*Universität Siegen, Institut für Werkstofftechnik, 57076 Siegen, Germany*

<sup>5</sup>*Humboldt-Universität zu Berlin, Institut für Physik, 12489 Berlin, Germany*

<sup>6</sup>*Università degli Studi di Salerno, Dipartimento di Ingegneria Industriale, 84084 Fisciano (SA), Italy*

(Dated: February 16, 2026)

The development of high-performance electron sources requires theoretical frameworks that accurately link the microscopic electronic properties of cathode materials to their macroscopic photoemission observables. Here, we present a many-body extension of the three-step photoemission model for semiconducting photocathodes, directly integrating the *GW* approximation and the solution of the Bethe-Salpeter equation on top of density functional theory (DFT). This approach overcomes the intrinsic limitations of standard DFT by explicitly accounting for quasiparticle and excitonic effects in the photoexcitation process. The quantum efficiency (QE) is evaluated by combining the *ab initio* absorption with an emission probability derived as an exciton-weighted average. We validate this model on representative alkali antimonides and demonstrate that a qualitative many-body description successfully captures complex spectral features that empirical models fail to reproduce. Furthermore, by incorporating macroscopic optical effects such as thin-film interference and polarization via Fresnel post-processing, we achieve quantitative agreement with experimental QE values without any adjustment. Minor discrepancies near the photoemission threshold are attributed to the idealized surface barrier adopted in the model and impurity effects in the samples, highlighting specific directions for future refinements. This work establishes a robust, parameter-free *ab initio* tool that bridges microscopic electronic correlation with macroscopic observables, providing a critical pathway for the rational design of next-generation electron sources.

## I. INTRODUCTION

The simulation of photoemission from solids has become an active research field in the last few years, driven by the need for high-quality electron sources in advanced applications such as free-electron lasers and particle accelerators [1, 2]. Over the last several decades, photoemission models have evolved significantly, moving from foundational phenomenological frameworks [3–5] to sophisticated first-principles schemes [6–8]. The pioneering work by Berglund and Spicer in 1964 [5] established the so-called three-step model, which conceptualizes photoemission in three sequential processes: (i) optical excitation generating photoelectrons, (ii) their scattering and transport to the surface, and (iii) their emission into the vacuum. Despite the success of the three-step model and its variants, particularly for polycrystalline or disordered cathodes [9, 10], modern applications require more sophisticated methods accounting for the electronic structure of the materials and the complex physics of thin-film heterostructures.

The increasing demand for high-quality photoemission predictions has boosted the development of parameter-free approaches that can be applied to any material,

independently of their synthesis and characterization. The one-step model specifically developed for metals [11] treats photoemission as a single quantum mechanical process. The total transition rate is calculated using Fermi’s golden rule, offering a quantitative explanation for the dependence of quantum efficiency (QE) on the polarization and angle of incidence of the incoming radiation. Inelastic collisions undergone by energetic electrons are explicitly incorporated via an effective scattering length. This model has been successfully applied to evaluate the emission from various metallic surfaces [6, 11, 12] even under *operando* conditions [13].

The model proposed by Jensen and coworkers in the early 2000s [14] aimed at improving the description of the intrinsic emittance of metal photocathodes beyond simple analytical methods. This framework has been subsequently extended to treat semiconductors, explicitly including band bending, phonon scattering mechanisms, effective mass differences, and the characteristic absence of electrons in the conduction band at rest conditions [15]. This model was successfully applied to Cs<sub>3</sub>Sb [15, 16], an established semiconducting photocathode for particle accelerators [17–19], and to its ternary sibling CsK<sub>2</sub>Sb [20].

The integration of photoemission models into *ab initio* workflows has substantially enhanced their predictive power. In the scheme proposed by Antoniuk et al. [7], the electronic structure is computed from density-functional theory (DFT), and the emission probability is

\* richard.schier@uni-jena.de

† caterina.cocchi@uni-jena.de

determined using Fermi's golden rule, neglecting scattering effects. A subsequent recipe proposed by Nangoi et al. [21] enhances the description of the second step by incorporating coherent electron-phonon scattering. These DFT-based photoemission models enable efficient material screening [22, 23] and a systematic assessment of structural or chemical modifications even in complex geometries such as heterostructures and alloys [24, 25].

On the downside, these pure DFT-based approaches suffer from crucial limitations in reproducing the electronic structure and the optical properties of semiconducting photocathodes. Relying on semi-local exchange-correlation functionals and on the independent-particle approximation for evaluating optical transitions, they treat particle interactions in a mean-field fashion, neglecting electron-electron and electron-hole correlations that are usually vital for a reliable description of photoemission. The adopted simplifications not only require *ad hoc* shifts of the electronic bands to match experiments [7] but also overshadow the fundamental many-body nature of the photoexcitation process in semiconductors [26–30].

In this work, we provide a many-body extension of the DFT-based three-step model for photoemission, integrating perturbation theory techniques such as the  $GW$  approximation for the electronic self-energy and the Bethe-Salpeter equation to describe (bound) excitons. Adopting an energy-dependent transmission probability, we derive the spectral response for a series of (multi-)alkali antimonide semiconductors and benchmark our predictions against experimental quantum efficiency measurements. While the output of this workflow already contains all qualitative features probed in experiments, quantitative predictions can be achieved from a Frenel-based supervised post-processing of the emission function, including macroscopic parameters such as sample thickness and incidence angle. Our findings bridge the gap between microscopic electronic structure calculations and macroscopic photoemission observables, providing an invaluable tool for the rational optimization of photocathode materials for particle accelerators.

## II. METHODS

Before introducing the proposed many-body extension of the *ab initio* three-step photoemission model, we review the formalism of DFT [31] and many-body perturbation theory (MBPT) [32] as the fundamental basis of our development (Sec. II A). This section is mainly addressed to an audience that is not familiar with these approaches and can be skipped by experienced readers. In Sec. II B, we provide the experimental settings employed to prepare the photocathode samples and to measure their photoemission yield.

### A. Theoretical Background

In the Kohn-Sham (KS) implementation of DFT [33], the fully interacting many-body problem is mapped by a fictitious system of independent particles, ruled by Schrödinger-like equations

$$\hat{h}^{KS} |\phi_{nk}\rangle = \epsilon_{nk}^{KS} |\phi_{nk}\rangle. \quad (1)$$

The KS Hamiltonian

$$\hat{h}^{KS} = \hat{t} + \hat{v}^{\text{eff}} = \hat{t} + \hat{v}^{\text{ext}} + \hat{v}^{\text{H}} + \hat{v}^{\text{xc}} \quad (2)$$

includes the single-particle kinetic energy operator  $\hat{t}$  and an effective potential  $\hat{v}^{\text{eff}}$ , which consists of the external potential ( $\hat{v}^{\text{ext}}$ ), accounting for the electron-nuclear attraction, the Hartree potential ( $\hat{v}^{\text{H}}$ ), capturing the classical repulsion experienced by an electron in a negative charge distribution, and the exchange-correlation (xc) potential ( $\hat{v}^{\text{xc}}$ ), embedding electronic interactions beyond the classical picture. Since the exact form of  $\hat{v}^{\text{xc}}$  is unknown, it must be approximated. The quality of this approximation ultimately determines the accuracy of the resulting electronic structure. While semi-local functionals are known to dramatically underestimate the fundamental gap of solids even by a factor of 2, hybrid functionals mitigate this issue but at substantially higher computational costs [34], which become unaffordable for large and complex systems or for screening an extended configurational space. Meta-GGA functionals [35] represent a reasonable compromise between accuracy and computational costs, even for photocathode materials [34, 36]. However, the numerical instabilities that are still present in many implementations require special care in high-throughput applications [37, 38].

The  $GW$  approximation [39] is the state-of-the-art method to calculate the electronic structure of solids, overcoming the infamous “band-gap problem” of DFT [40]. In the perturbative  $G_0W_0$  approach, the electronic self-energy is calculated as

$$\Sigma(r, r', \omega) = \frac{i}{2\pi} \int G_0(r, r', \omega + \omega') W_0(r, r', \omega') e^{i\omega' \eta} d\omega', \quad (3)$$

where  $G_0$  is the single-particle Green's function computed on top of DFT and  $W_0$  is the Coulomb potential screened by the frequency-dependent dielectric function of the material,  $\epsilon(\omega)$ . The self-energy computed from Eq. (3) enters the quasi-particle (QP) equation for the electron energies,

$$\epsilon_{nk}^{\text{QP}} = \epsilon_{nk} + Z_{nk} [\Re \Sigma_{nk}(\epsilon_{nk}) - V_{nk}^{\text{xc}}], \quad (4)$$

where the renormalization factor  $Z_{nk}$  accounts for the energy-dependence of the self-energy from which the contribution from the xc potential,  $V_{nk}^{\text{xc}} = \langle \phi_{nk} | \hat{v}^{\text{xc}} | \phi_{nk} \rangle$ , must be subtracted.

To calculate optical excitations including excitonic effects, the equation of motion of the electron-hole correlation function, known as the Bethe-Salpeter equation

(BSE) [41], must be solved. In the context of electronic-structure simulations, the BSE is mapped into the eigenvalue problem

$$\sum_{v'c'\mathbf{k}'} H_{vck, v'c'\mathbf{k}'}^{\text{BSE}} A_{v'c'\mathbf{k}'}^{\lambda} = E^{\lambda} A_{vck}^{\lambda}, \quad (5)$$

where the indices  $v$  and  $c$  label valence and conduction states, respectively. The two-particle BSE Hamiltonian

$$\hat{H}^{\text{BSE}} = \hat{H}^{\text{diag}} + 2\hat{H}^{\text{x}} + \hat{H}^{\text{c}} \quad (6)$$

consists of three terms. The diagonal term ( $\hat{H}^{\text{diag}}$ ) describes vertical electronic transitions, the exchange term ( $\hat{H}^{\text{x}}$ ), which is multiplied by 2 assuming spin-degenerate systems, accounts for the repulsive exchange interaction within the fermionic electron-hole pairs, while the direct term ( $\hat{H}^{\text{c}}$ ) includes the attractive electron-hole screened Coulomb interaction. The diagonalization of Eq. (5) delivers excitation energy eigenvalues  $E^{\lambda}$  and eigenvectors  $A^{\lambda}$ , which contain information about the oscillator strength and composition of the  $\lambda$ -th excited state.  $A^{\lambda}$  enter the expression of the imaginary part of the macroscopic dielectric tensor,

$$\Im\epsilon_M = \frac{8\pi^2}{\Omega} \sum_{\lambda} |\mathbf{t}^{\lambda}|^2 \delta(\omega - E^{\lambda}), \quad (7)$$

through the transition coefficients

$$\mathbf{t}^{\lambda} = \sum_{vck} A_{vck}^{\lambda} \frac{\langle \phi_{vk} | \hat{\mathbf{p}} | \phi_{ck} \rangle}{\epsilon_{ck}^{\text{QP}} - \epsilon_{vk}^{\text{QP}}}. \quad (8)$$

The momentum matrix elements in the numerator of Eq. (8) couple transitions between occupied ( $v$ ) and unoccupied ( $c$ ) KS states. The ideally infinite number of conduction states assumed in the sum is numerically converged to a finite value. Finally, the contribution of specific single-particle transitions to the electron-hole state is quantified by the so-called *exciton weights* for holes

$$w_{v\mathbf{k}}^{\lambda} = \sum_c |A_{vck}^{\lambda}|^2 \quad (9)$$

and electrons

$$w_{c\mathbf{k}}^{\lambda} = \sum_v |A_{vck}^{\lambda}|^2. \quad (10)$$

## B. Experimental Setup

The experimental data for the ternary alkali antimonides were collected in the photocathode laboratory at Helmholtz-Zentrum Berlin für Materialien und Energie GmbH (HZB) [42]. The photocathodes are prepared on a Mo substrate to meet the high thermal and electrical requirements necessary for operation in a superconducting radio-frequency accelerator. The Na-K-Sb sample TWH25 (Fig. 4a) was prepared by simultaneous

deposition of all three materials (triple evaporation) from thermal effusion cells [43], while the Cs-K-Sb photocathode G002 (Fig. 4b) was grown from deposition of a pure Sb layer and subsequent co-deposition of the alkali metals from dispensers [44, 45]. These samples were prepared, stored, and characterized under ultra-high vacuum conditions to avoid any degradation of the photocathodes due to residual gases. During preparation, the QE was used as feedback to optimize the growth parameters [42, 43].

To perform spectrally resolved QE measurements, the photocathodes were illuminated by a monochromatic light source, consisting of a Xenon lamp and a monochromator. The photocurrent was measured by a picoammeter attached to a copper wire approximately 10 mm away from the photocathode surface. The wire was positively biased and acted as a pick-up anode [46]. Under these conditions, the QE was determined by

$$\text{QE} = \frac{I_e h c}{P_{\gamma} \lambda e} \quad (11)$$

where  $I_e$  is the measured current,  $P_{\gamma}$  the optical power, and  $\lambda$  the wavelength of the incoming radiation.

## III. PHOTOEMISSION MODEL FROM AB INITIO MANY-BODY THEORY

The photoemission scheme from *ab initio* many-body theory proposed in this work is based on the three-step model originally formulated by Berglund and Spicer [3, 5]. In this framework, the photoemission process is decomposed into three sequential steps: First, an incident photon excites an electron from an initially occupied valence state to the conduction band. In the second step, the excited electron travels through the crystal toward the surface, potentially undergoing scattering events with other electrons and/or with phonons. In the third and final stage, the electron overcomes the surface potential barrier and is emitted.

The proposed model implements the above-mentioned steps in the framework of DFT and MBPT, see Fig. 1. The starting point is the definition of the crystal structure, either tabulated or retrieved from computational or experimental databases. In the latter scenario, *ad hoc* routines embedded in the in-house developed **Python** library **aim<sup>2</sup>dat** offer an effective and well-tested tool for data mining [38]. Following the input setup, the structures are relaxed, including both lattice optimization and interatomic force minimization, as discussed in previous work [29, 30]. The final DFT step includes a self-consistent field calculation as a starting point for MBPT, including both the QP correction to the electronic structure from  $G_0W_0$  (Eq. 4) and the solution of the BSE to compute the optical spectrum (Eq. 7) and excitonic weights (Eqs. 9 and 10). The  $G_0W_0$ +BSE results are post-processed to evaluate the excitation and emission probability, finally delivering the QE as discussed in detail below. To illustrate the physical significance and the

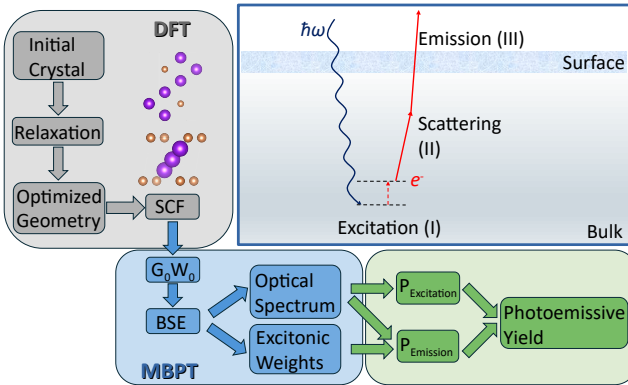


FIG. 1. Schematic overview of the three-step model for photoemission implemented from *ab initio* many-body theory. The colored blocks illustrate each computational step, including DFT calculations of the ground-state properties (grey), MBPT runs ( $G_0W_0$ +BSE) to access excited state properties (blue), and final post-processing to compute the photoemission yield (green).

main ingredient entering each step, we take as an example hexagonal  $K_3Sb$ , an alkali antimonide crystal thoroughly characterized from DFT and MBPT in previous work [29].

### A. Step 1: Photoexcitation

The excitation probability quantifies the first step of photoemission. The standard expression of the imaginary part of the macroscopic dielectric function obtained by solving the BSE (Eq. 7) is conveniently reformulated as follows [47]:

$$\Im\epsilon_M = \frac{4\pi^2}{\pi\Gamma\Omega} \sum_{\lambda} |\mathbf{t}_{\lambda}|^2 \left( \frac{\Gamma^2}{(\omega - E_{\lambda})^2 + \Gamma^2} - \frac{\Gamma^2}{(\omega + E_{\lambda})^2 + \Gamma^2} \right). \quad (12)$$

In contrast to the general form in Eq. (7), where the electron excitation is modeled by a  $\delta$ -function, Eq. (12) includes a finite Lorentzian broadening  $\Gamma$  and explicitly decouples excitation and de-excitation processes.  $E_{\lambda}$  and  $\mathbf{t}_{\lambda}$  are the excitation energies and transition coefficients defined in Eq. (5) and Eq. (8), respectively.

The macroscopic dielectric function defined in Eq. (12) is a tensor, with the number of inequivalent components and their magnitude dictated by crystal symmetry. While all the elements of  $\Im\epsilon_M(\omega)$  are obtained by diagonalizing Eq. (5), experiments probing photocathode emission are typically insensitive to the polarization direction. To mimic this scenario and assuming that off-diagonal contributions are absent or negligible, we average over all diagonal components and define the photoexcitation probability as the trace of the imaginary part of the dielectric function normalized to its absolute maxi-

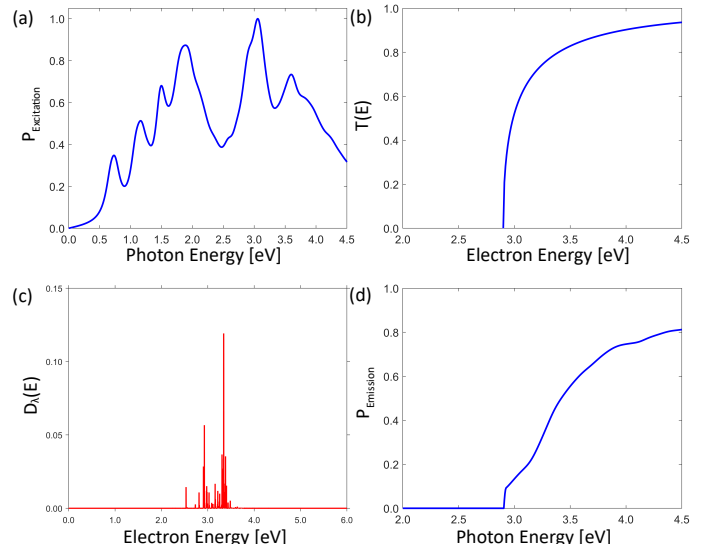


FIG. 2. Results for  $K_3Sb$ : (a) Optical absorption averaged over components [29], (b) probability of emission depending on the energy of the excited electron, with onset from experiment [3], (c) exemplary energy distribution of an excited electron at 3.6 eV, and (d) total calculated emission probability by photon energy.

mum in the considered spectral region:

$$P_{\text{Excitation}}(\omega) = \frac{\Im\epsilon_M^{\text{avg}}(\omega)}{\max_{\omega}[\Im\epsilon_M^{\text{avg}}(\omega)]}. \quad (13)$$

The excitation probability of hexagonal  $K_3Sb$ , calculated from Eq. (13) including both in-plane and out-of-plane contributions from the dielectric tensor [29], is shown in Fig. 2(a).

### B. Step 2: Electron Transport and Scattering

Electron transport and scattering events included in the second step of Spicer's model are treated here as elastic processes, neglecting any dissipation effects. This assumption, already adopted by Antoniuk et al. [7], is justified both by material properties and computational goals. The proposed MBPT-based framework targets semiconducting photocathodes, where electron-electron scattering mechanisms are negligible. While electron-phonon scattering is the primary collision mechanism in semiconductors, in alkali antimonides it leads to electronic band renormalizations of the order of 100 meV [48], which corresponds to less than 1% of the expected emission yield [7]. Neglecting inelastic scattering and thus ignoring electron losses occurring during migration to the surface is expected to overestimate the QE. Since the primary goal of the current implementation is to predict the spectral dependence of the photoemission yield, which is predominantly governed by the energy-dependent probability of excitation (Step 1) and emission (Step 3 dis-

cussed below), skipping the transport step leads to a minimal impact while offering, on the other hand, a substantial reduction of computational costs.

Under this approximation, the QE is determined by the product of the excitation and emission probability,

$$\text{QE}(\omega) \propto P_{\text{Excitation}}(\omega) \cdot P_{\text{Emission}}(\omega), \quad (14)$$

consistent with the mathematical simplification adopted in the Dowell-Schmerge photoemission model [49]. Future extensions of the current development may lift this simplification and include scattering probabilities computed, for example, from Monte-Carlo simulations [48, 50, 51].

### C. Step 3: Emission Probability

The emission probability quantifies the fraction of charge carriers escaping the surface. Necessary ingredients for this assessment are the accurate determination of the vacuum potential  $V_0$ , either from the experimental work function or from DFT calculations on surface slabs [7, 36], and the potential barrier. Here, we adjust the onset to the measured work function and assume an idealized barrier described by a step function:

$$T(E) = \begin{cases} \frac{4\sqrt{E(E-V_0)}}{(\sqrt{E}+\sqrt{E-V_0})^2} & \text{for } E \geq V_0 \\ 0 & \text{for } E < V_0. \end{cases} \quad (15)$$

The transmission function  $T(E)$  adopted for hexagonal  $K_3Sb$  is shown in Fig. 2(b), where  $V_0 = 2.9$  eV matches the experimental value [3]. Below this threshold, no transmission is possible, while for  $E \geq V_0$ ,  $T(E)$  grows steeply and asymptotically according to

$$\lim_{E \rightarrow \infty} T(E) = 1. \quad (16)$$

The total emission probability,  $P_{\text{Emission}}(\omega)$ , is defined by convoluting  $T(E)$  with the energy distribution function,  $D_\lambda(E)$ , of the excited electron generated from the  $\lambda$ -th excitation.  $D_\lambda(E)$  represents the normalized probability of finding the photogenerated electron at the energy  $E$  and is determined by summing the  $\mathbf{k}$ -resolved electron weights computed from the BSE (Eq. 10) targeting QP states above the band gap:

$$D_\lambda(E) = \sum_{c=n_{\text{CBm}}}^{n_{\text{CBmax}}} \sum_{\mathbf{k}} w_{c\mathbf{k}}^\lambda \delta(E - \varepsilon_{c\mathbf{k}}^{QP}). \quad (17)$$

In Eq. (17), the first sum runs from the lowest conduction band ( $n_{\text{CBm}}$ ) to the uppermost unoccupied state included in the solution of the BSE ( $n_{\text{CBmax}}$ ). In the implemented workflow, QP energies are assigned via a rigid scissor shift corresponding to the QP correction to the fundamental gap from DFT. This numerical shortcut is validated by

full  $G_0W_0$  calculations (Fig. S2) and physically justified by  $T(E)$  being most sensitive to energy corrections near the emission threshold  $V_0$ .

An example of  $D_\lambda(E)$  computed for the excitation at 3.6 eV in hexagonal  $K_3Sb$  is shown in Fig. 2(c). The  $\delta$ -like shape of this function (Eq. 17) is reflected in the plot, displaying a charge-carrier distribution between 2.9 and 3.4 eV. Additional contributions at lower energies are non-zero but so much smaller in magnitude that they are not visible in Fig. 2(c).

For each excitation  $\lambda$  computed from diagonalizing Eq. (5) the associated emission probability defined as:

$$P_{\text{Emission}}^\lambda = \int_{E_{\text{CBm}}}^{E_{\text{max}}} T(E) D_\lambda(E) dE. \quad (18)$$

In Eq. (18), the lower integration boundary is the conduction band minimum ( $E_{\text{CBm}}$ ) while the upper limit ( $E_{\text{max}}$ ) corresponds to the available energy range from the solution of the BSE. These limits are the energy values related to  $n_{\text{CBm}}$  and  $n_{\text{CBmax}}$  defined in Eq. (17). To compute  $P_{\text{Emission}}(\omega)$  entering Eq. (14),  $P_{\text{Emission}}^\lambda$  must be weighted by the contribution of the  $\lambda$ -th exciton to the total spectrum  $\mathcal{S}(\omega) \equiv \Im \epsilon_M(\omega)$  [see Eq. (12)]. To this end, we introduce the exciton-selective excitation probability

$$p_\lambda(\omega) = \frac{\mathcal{S}_\lambda(\omega)}{\mathcal{S}(\omega)}, \quad (19)$$

where

$$\mathcal{S}_\lambda(\omega) = \frac{4\pi^2}{\pi\Gamma\Omega} |\mathbf{t}_\lambda|^2 \left( \frac{\Gamma^2}{(\omega - E_\lambda)^2 + \Gamma^2} - \frac{\Gamma^2}{(\omega + E_\lambda)^2 + \Gamma^2} \right), \quad (20)$$

to calculate the overall emission probability

$$P_{\text{Emission}}(\omega) = \sum_{\lambda} p_\lambda(\omega) P_{\text{Emission}}^\lambda, \quad (21)$$

representing the probability that an absorbed photon with frequency  $\omega$  generates an emitted electron.

$P_{\text{Emission}}(\omega)$  computed for hexagonal  $K_3Sb$  is visualized in Fig. 2(d). The steep onset around 2.9 eV, stemming from the stepwise potential barrier [Fig. 2(b)], is modulated immediately above threshold, for  $E > 3.0$  eV. The monotonic increase persists up to about 4.0 eV, when the slope of the emission yield decreases drastically compared to the lower-energy region ( $3.0 \leq E \leq 4.0$ ).

The QE is computed from the convolution of  $P_{\text{Emission}}(\omega)$  with the excitation probability derived from the imaginary part of the macroscopic dielectric function (Eq. 12). This leads to the modulated probability that a photon with frequency  $\omega$  creates an exciton, which, after dissociation, generates an emitted electron (Eq. 14):

$$P_{\text{Yield}}(\omega) = P_{\text{Excitation}}(\omega) \cdot P_{\text{Emission}}(\omega). \quad (22)$$

#### IV. MODEL VALIDATION: ALKALI ANTIMONIDE PHOTOCATHODES

We validate the developed three-step model from *ab initio* many-body theory against experimental photoemission data available in the literature. In this comparison, we align the simulated QE to the maximum experimental value. This empirical step is necessary to connect the microscopic description provided by our *ab initio* model to measurements performed on films with a finite thickness. Here, we focus on the qualitative description of photoemission yield, adopting quantitative refinements for comparison with our experimental data on  $\text{Cs}_3\text{Sb}$  (see Sec. VI).

We start with hexagonal  $\text{K}_3\text{Sb}$ , a semiconducting photocathode measured by Spicer in 1958 [3] and used in Sec. III to illustrate the implemented steps in the model. This material exhibits a rich optical absorption spectrum in the visible region [29], giving rise to a modulated photoemission curve that is fully captured by our *ab initio* simulations [Fig. 3(a)]: The steep increase of the QE up to its maximum value of 0.07 reached at 3.6 eV is followed by a smoother decrease above 4.0 eV, due to the reduction of the optical absorption in this energy region [29].

The most noticeable difference between the experimental data and our computational prediction is at the onset, where the model predicts a much sharper transition than the measurement. This characteristic is a direct consequence of describing the emission barrier as a step function [Fig. 2(b)]. Moreover, as already noted by Spicer [3, 52], photoemission from  $\text{K}_3\text{Sb}$  is significantly influenced by impurities, leading to a non-zero smearing of the QE near the onset. Since our *ab initio* calculations are performed for an ideal  $\text{K}_3\text{Sb}$  bulk crystal [29], these physical effects are not included. It is also worth noting that the empirical version of Spicer's model, which could successfully describe the photoemission yield of cubic alkali antimonide crystals [3], is unable to reproduce the experimental QE of  $\text{K}_3\text{Sb}$  [3, 52], due to the complex band structure stemming from its hexagonal lattice. The overall very good performance of our model demonstrates the need for an accurate description of the electronic structure to properly simulate the photoemission yield of this material. Future refinements, including defects and impurities, are expected to provide an even closer agreement with the measurements.

Next, we compare the simulated and measured QE for another hexagonal alkali antimonide, namely  $\text{Na}_3\text{Sb}$  [Fig. 3(b)]. This material exhibits a high threshold for intrinsic photoemission above 3.5 eV, given by its band gap of approximately 1.1 eV and its electron affinity around 2.4 eV [3, 52]. After a steep increase, the QE reaches its maximum of 0.02 at about 4.4 eV. This behavior is well reproduced by our *ab initio* many-body model, with the computed QE curve modulated by the underlying optical absorption [29], see Fig. S3(b). At low energies, the experimental photoemission yield of  $\text{Na}_3\text{Sb}$  is affected by impurities [3, 52], leading to non-zero values below the

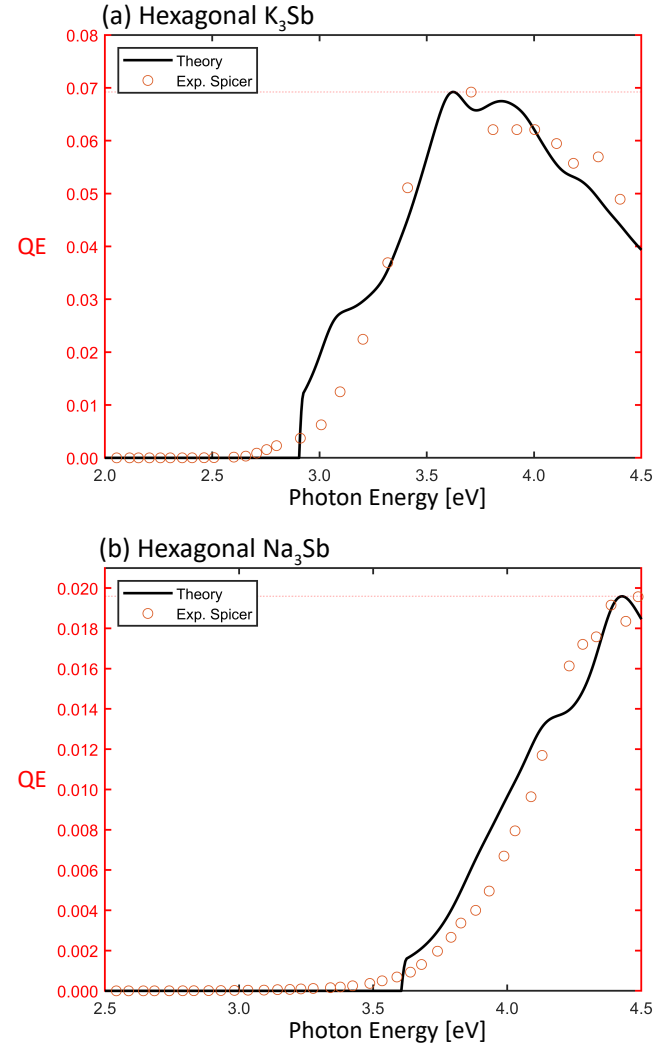


FIG. 3. Results for binary crystals composed of K/Na and Sb, matched against experimental data from Spicer[3]. The dotted bars indicate the QE value used for aligning the *ab initio* many-body prediction to the experimental data.

onset and to a smoother increase compared to our simulation of the ideal crystal and the emission barrier approximated by a step-function. Similar to  $\text{K}_3\text{Sb}$ , Spicer's empirical model is incapable of fitting the measurement, due to the non-trivial band structure of hexagonal  $\text{Na}_3\text{Sb}$ .

#### V. PHOTOEMISSION PREDICTIONS FOR TERNARY ALKALI ANTIMONIDES

After the successful benchmark of our *ab initio* many-body method for calculating photoemission yield against experimental data available from the literature for binary alkali antimonides, we put it to the test for ternary compositions ( $\text{Na}_2\text{KSb}$  and  $\text{CsK}_2\text{Sb}$ ), representing state-of-the-art semiconducting materials employed for pho-

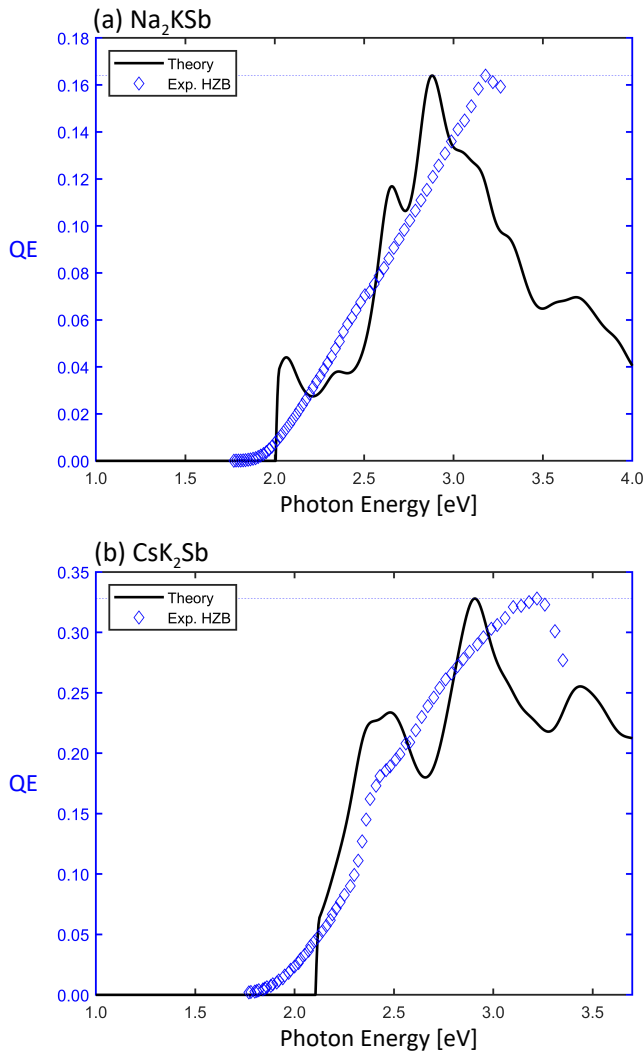


FIG. 4. QE of cubic  $\text{Na}_2\text{KSB}$  and  $\text{CsK}_2\text{Sb}$  crystals measured at HZB and computed from the proposed *ab initio* many-body photoemission model. The dotted horizontal bars indicate the QE value used to align the calculated spectrum to the experimental data.

tocathodes in particle accelerators [2, 53, 54]. For this comparison, we take as a reference our spectra measured at HZB.

$\text{Na}_2\text{KSB}$  is known for its stability [55–57] and  $\text{QE} > 10\%$  in the visible-to-infrared range [58], as confirmed by our measurements [Fig. 4(a)]. The investigated sample exhibits an emission threshold around 2.0 eV, with the QE rising steeply toward a maximum at 3.2 eV. The experimental curve shows subtle changes in slope at 2.5 eV and 3.0 eV, hinting at an underlying spectral modulation. The quantum yield computed from first principles reproduces well the experimental trend while providing enhanced resolution on these individual features. As discussed for the binary compounds above, the wealth of details in the simulated QE stems directly from the opti-

cal absorption spectrum calculated from GW+BSE [27], see Fig. S4(a). Given the relatively low vacuum potential of this material [Fig. S1(d)], most optical excitations in  $\text{Na}_2\text{KSB}$  effectively modulate the emission probability [Fig. S4(b)] and, ultimately, the final QE prediction [Fig. 4(a)].

The systematic energy shift of about 100 meV between the measured and simulated QE of  $\text{Na}_2\text{KSB}$  [Fig. 4(a)] can be ascribed to both intrinsic and extrinsic experimental conditions, such as defects, polycrystallinity, and temperature effects, noting, however, that the numerical accuracy of the GW+BSE results is of the same order of magnitude [27]. While the experimental curve appears smoother than the simulation due to measurement-induced broadening, the *ab initio* results successfully capture the fundamental spectral profile. When accounting for this difference in resolution and the above-mentioned energy shift, the agreement between experimental data and many-body prediction for  $\text{Na}_2\text{KSB}$  is excellent.

We conclude this analysis by comparing the measured and simulated QE of  $\text{CsK}_2\text{Sb}$ . This material is one of the most popular bialkali antimonides used for photocathodes in particle accelerators [2, 44, 53]. As shown in Fig. 4(b), it features a large QE between 10% and 35% across the entire visible range above threshold ( $\sim 2.0$  eV). Interestingly, the measurement [44] features the same spectral modulation predicted by theory. In particular, the first relative maximum, followed by a narrow plateau between 2.4 and 2.5 eV, appears in both experiment and simulations, with only a minimal energetic shift of a few tens of meV. At higher energies, the *ab initio* prediction features a minimum at 2.6 eV, which is only hinted at by a change of slope in the measurement. Above 2.6 eV, both the experimental and theoretical QE increase steeply, reaching the absolute maximum at 3.2 eV and 2.9 eV, respectively, and reproducing the subsequent sudden drop in yield [Fig. 4(b)].

The characteristic features of the QE curve predicted from first principles can be traced back to the optical spectrum computed for  $\text{CsK}_2\text{Sb}$  from GW+BSE, where two peaks appear at 2.4 eV and 2.9 eV [26]. Although additional absorption maxima are present at lower energies [Fig. S4(c)], they are both below the emission threshold determined by the vacuum potential [Fig. S1(e)] and thus do not enter the calculation for the emission probability [Fig. S4(d)]. The excellent agreement between theory and experiments for the first peak at 2.4 eV can be ascribed to the lower accuracy expected for the GW/BSE calculations of transitions above the absorption onset ( $E > 1.5$  eV) and thus targeting high conduction states that not included in the solution of the BSE [26]. Refinements of the GW+BSE calculations on  $\text{CsK}_2\text{Sb}$ , such as extending the energy range of unoccupied states included in the simulation, can be applied to improve the QE in this high-energy region.

## VI. QUANTITATIVE QE PREDICTIONS FOR CESIUM ANTIMONIDE

In the results discussed so far, the *ab initio* predicted QE was manually aligned to the maximum of the measured curve (Fig. 3 and Fig. 4). While this approach is fully reasonable to validate the method and obtain a qualitative comparison of the main spectral features, it has a limited predictive power in realistic conditions where the independent measurements may deliver different results, or when there is no reference to compare with. In the following, we examine the photoemission yield of cubic  $\text{Cs}_3\text{Sb}$ , likely the most popular alkali antimonide photocathode material [2, 53, 59]. We compare our *ab initio* results with four experimental datasets, representing a diverse range of growth techniques and sample qualities: Spicer's pioneering measurements [3], recent benchmarks from Karkare's group at Arizona State University (ASU) [8], data collected at Cornell University [60], and measurement performed at HZB [61].

All the experimental results presented in Fig. 5 exhibit a smooth onset around 2.0 eV. While the measurements from ASU extend only up to 2.5 eV [8], the remaining three datasets follow a similar energy-dependent trend up to approximately 2.7 eV. Between 2.3 eV and 2.7 eV, the Cornell sample shows the steepest increase, reaching a maximum QE of about 13% close to 3.0 eV. The highest emission yield is scored by the HZB sample (QE  $\sim$ 17% at 2.95 eV), while Spicer's measurements follow a slower monotonic increase, culminating in a maximum QE of approximately 14% at 3.5 eV (Fig. 5).

A common feature of the simulated results discussed so far is a sharper onset compared to the experimental curves. This can be attributed to several factors inherent to real-world photocathodes. Primarily, alkali antimonide surfaces are characterized by chemical roughness, inducing spatial variations in the work function on the order of 0.3–0.4 eV [59]. When combined with the typical monochromator bandwidth of 5–10 nm used in the measurements, these effects naturally broaden and soften the sharp excitonic features and step-like thresholds predicted by our theory at 0 K. On the other hand, the variations among the datasets shown in Fig. 5 can be attributed to the growth method. While traditional co-deposited films frequently exhibit a “knee” feature around 2.1 eV followed by a defect-driven tail [62], quasi-epitaxial films, such as those grown on  $\text{SrTiO}_3$  at ASU [8] or via deposition-recrystallization at HZB [61], show a much more gradual increase in QE. These quasi-epitaxial samples are typically ultrathin (10–15 nm) and more closely resemble the ideal crystal structure used in the many-body calculations.

Finally, it is worth noting that, while the traditional photoemission threshold for  $\text{Cs}_3\text{Sb}$  is often reported at about 2.1 eV, recent photoemission electron spectroscopy measurements have suggested a significantly lower work function of about 1.5 eV [63]. In this context, the threshold features in spectral response curves may not

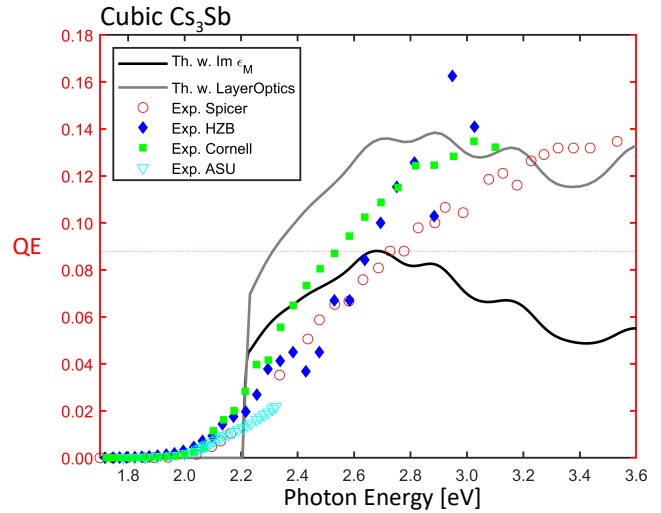


FIG. 5. Results for cubic  $\text{Cs}_3\text{Sb}$ , compared against experimental data from Spicer [3] as well as measurements performed at HZB [61], Cornell University [60] and ASU [8]. The dotted bars indicate the QE value used to align the *ab initio* many-body prediction with the experimental data. A quantitative prediction for a 9 nm-thick thin film calculated with LayerOptics is provided without manual alignment of the QE.

solely represent the vacuum barrier, but rather specific structures in the density of states or excitonic transitions. This view is supported by the detailed energy distribution functions derived from our BSE calculations [26, 27, 29].

The wealth of experimental data available for  $\text{Cs}_3\text{Sb}$  and the inherent differences in the QE curves, arising from the different preparation techniques, underscore the limitations of manually aligning the photoemission yield computed from first principles. In Fig. 5, this adjustment was performed in the spectral region between 2.5 and 2.7 eV, where the results from Spicer, HZB, and Cornell are in closest proximity. However, this arbitrary choice introduces an inevitable mismatch with one more datasets. Up to 2.4 eV, our *ab initio* prediction overestimates the QE compared to all experimental references. At higher energies, the steep yield increase reported in the Cornell sample is not featured by the calculated curve, which remains in better agreement with Spicer's and HZB data up to 2.7 eV. The region  $2.7 \text{ eV} < E < 3.6 \text{ eV}$  is the most problematic for the theoretical result, which underestimates all experimental curves by at least a factor of 2 (Fig. 5). This discrepancy can be ascribed to the large number of electronic bands involved in such high-energy transitions, which were not fully included in the BSE calculation originally performed to investigate the optical absorption of  $\text{Cs}_3\text{Sb}$  [26].

The discrepancies discussed above motivate us to enhance the predictive power of our model by post-processing the dielectric function with Fresnel equations,

incorporating macroscopic parameters such as the film thickness, the angle of incidence, and the light polarization. This procedure is implemented in the **Python** package **LayerOptics** [64], a tool designed to handle complex optical geometries by rotating the dielectric tensor to match specific surface orientations [65–67]. While the cubic symmetry of  $\text{Cs}_3\text{Sb}$  does not require the advanced features of **LayerOptics** for anisotropic materials [64], its application allows us to assume normal incidence for the incoming radiation and to account for a film thickness of 9 nm, matching the specifications of the sample grown at Cornell [60].

The excitation probability assumed in the Maxwell formalism of **LayerOptics** is defined as:

$$\tilde{P}_{\text{Excitation}}(\omega) = 1 - (R(\omega) + T(\omega)), \quad (23)$$

where  $R(\omega)$  and  $T(\omega)$  are the calculated reflectance and transmittance of the sample, respectively. Substituting  $\tilde{P}_{\text{Excitation}}$  into the expression for the photoemission yield, we obtain

$$\tilde{P}_{\text{Yield}}(\omega) = \tilde{P}_{\text{Excitation}}(\omega) \cdot P_{\text{Emission}}(\omega). \quad (24)$$

This result is the quantitative counterpart of the photoemission yield introduced in Eq. (22), allowing for a direct comparison with experimental data without the need for manual scaling or external parameters.

The QE of  $\text{Cs}_3\text{Sb}$  predicted with **LayerOptics** is in much better agreement with the experimental data (gray curve in Fig. 5). The maximum featured at approximately 14% is remarkably close to both the Cornell and HZB measurements. Notably, the **LayerOptics** notably enhances the prediction of Spicer's QE between 3.0 and 3.5 eV. Beyond the quantitative improvement, this post-processing also enhances the qualitative spectral behavior. While the low-energy portion of the curve is essentially translated to higher QE values, the range between 2.7 and 3.2 eV no longer exhibits the systematic envelope reduction that caused the mismatch between the measurements and the unprocessed *ab initio* results. In particular, the theoretical curve refined with **LayerOptics** closely follows the profile recorded at Cornell. Moreover, it better replicates the spectral increase observed in the HZB and Spicer datasets, despite the persistent overestimation in the 2.2–2.7 eV range.

This improved description demonstrates that accounting for macroscopic optical effects, specifically the interference and polarization-dependent reflectance within the thin film, is critical for bridging microscopic many-body theory with realistic photoemission observables. By incorporating the experimental geometry and film thickness, we move from a qualitative spectral analysis to a truly predictive quantitative framework.

## VII. SUMMARY AND CONCLUSIONS

In summary, we presented an *ab initio* many-body extension of the three-step photoemission model for semi-

conducting photocathodes, directly integrating the *GW* approximation and the solution of the BSE on top of DFT. This methodology successfully links the microscopic electronic structure of the materials, including quasiparticle and excitonic effects, with the QE. We validated our model against experimental data for binary and ternary alkali antimonides, demonstrating very good agreement with measurements obtained from independent groups. Our predictions offer in-depth insight into the spectral response of the crystals, capturing complex features, such as electronic self-energy and excitonic transitions, that are intrinsic to photo-excitation and cannot be captured by DFT alone.

The successful transition from a qualitative spectral analysis to a quantitative prediction of the QE using the post-processing tool **LayerOptics** allowed us to move beyond empirical alignment, yielding quantitative predictions that accurately match absolute QE values with remarkable accuracy. This demonstrates that the combination of many-body perturbation theory and classical Fresnel optics provides a complete framework for describing the photoemission process.

In conclusion, this work successfully bridges the gap between an accurate microscopic characterization of the spectral response of semiconductors and the macroscopic photoemission process. The integration of MBPT methods overcomes the accuracy limitations of previous models based on semi-local DFT and provides a robust, parameter-free tool for predicting the spectral characteristics of semiconducting photocathodes, opening the path for the rational design and optimization of next-generation electron sources.

Future work will focus on quantitative improvements, such as the incorporation of scattering contributions via Monte-Carlo methods, more realistic descriptions of potential barriers, and the inclusion of surface and defects in the atomistic modeling of the samples to better mimic realistic conditions. From the experimental side, the development of this accurate model stimulates refinements in the growth and characterization procedure, enabled, for example, via epitaxial growth. By providing an exemplary bridge between atomistic quantum theory and state-of-the-art experiments, this work represents a milestone in photocathode development.

## ACKNOWLEDGMENTS

The authors thank Sonal Mistry and Martin Schmeißer for valuable discussions. This work was funded by the German Research Foundation (DFG), Project No. 490940284. Computational resources were provided by the High-Performance Computing Center at the University of Oldenburg through the clusters CARL and ROSA, funded by the Lower Saxony Ministry for Science and Culture and by the DFG (Project Nr. INST 184/157-1 FUGG and INST 184/225-1 FUGG, respectively).

## AUTHOR CONTRIBUTIONS

R.S. and C.C. developed the theoretical framework. R.S. implemented the computational method, performed all *ab initio* simulations, prepared the figures, curated the data, and wrote the original manuscript draft. C.C. conceptualized the work, validated the results, and final-

ized the manuscript. J.D., C.W., J.K., and T.K. designed the experiments and developed the apparatus for spectral response. J.D., C.W., and J.K. performed the measurements. J.D., C.W., T.K., and A.G. analyzed and interpreted the experimental data. C.C. and T.K. acquired the resources. All authors contributed to the discussion of the results, provided critical feedback, and reviewed the final manuscript.

---

[1] D. Filippetto, P. Musumeci, R. Li, B. J. Siwick, M. Otto, M. Centurion, and J. Nunes, Ultrafast electron diffraction: Visualizing dynamic states of matter, *Rev. Mod. Phys.* **94**, 045004 (2022).

[2] J. Schaber, R. Xiang, and N. Gaponik, Review of photocathodes for electron beam sources in particle accelerators, *J. Mater. Chem. C* **11**, 3162 (2023).

[3] W. E. Spicer, Photoemissive, photoconductive, and optical absorption studies of alkali-antimony compounds, *Phys. Rev.* **112**, 114 (1958).

[4] E. O. Kane, Theory of photoelectric emission from semiconductors, *Phys. Rev.* **127**, 131 (1962).

[5] C. N. Berglund and W. E. Spicer, Photoemission studies of copper and silver: Theory, *Phys. Rev.* **136**, A1030 (1964).

[6] B. Camino, T. Noakes, M. Surman, E. Seddon, and N. Harrison, Photoemission simulation for photocathode design: Theory and application to copper and silver surfaces, *Comp. Mater. Sci.* **122**, 331 (2016).

[7] E. R. Antoniuk, Y. Yue, Y. Zhou, P. Schindler, W. A. Schroeder, B. Dunham, P. Pianetta, T. Vecchione, and E. J. Reed, Generalizable density functional theory based photoemission model for the accelerated development of photocathodes and other photoemissive devices, *Phys. Rev. B* **101**, 235447 (2020).

[8] P. Saha, O. Chubenko, G. S. Gevorkyan, A. Kachwala, C. J. Knill, C. Sarabia-Cardenas, E. Montgomery, S. Poddar, J. T. Paul, R. G. Hennig, *et al.*, Physically and chemically smooth cesium-antimonide photocathodes on single crystal strontium titanate substrates, *Appl. Phys. Lett.* **120**, 194102 (2022).

[9] D. Dimitrov, G. Bell, J. Smedley, I. Ben-Zvi, J. Feng, S. Karkare, and H. Padmore, Modeling quantum yield, emittance, and surface roughness effects from metallic photocathodes, *J. Appl. Phys.* **122** (2017).

[10] P. Saha, O. Chubenko, J. Kevin Nangoi, T. Arias, E. Montgomery, S. Poddar, H. A. Padmore, and S. Karkare, Theory of photoemission from cathodes with disordered surfaces, *J. Appl. Phys.* **133** (2023).

[11] S. Karkare, W. Wan, J. Feng, T. C. Chiang, and H. A. Padmore, One-step model of photoemission from single-crystal surfaces, *Phys. Rev. B* **95**, 075439 (2017).

[12] G. Adhikari, P. Riley, and W. Schroeder, Spectral characterization of a rh (110) photocathode: Band structure interpretation, *AIP Adv.* **9**, 065305 (2019).

[13] W. A. Schroeder and G. Adhikari, Evaluation of photocathode emission properties in an electron gun: one-step photoemission from bulk band to vacuum states, *New. J. Phys.* **21**, 033040 (2019).

[14] K. L. Jensen, P. O'Shea, D. Feldman, and N. A. Moody, Theoretical model of the intrinsic emittance of a photocathode, *Appl. Phys. Lett.* **89**, 224103 (2006).

[15] K. L. Jensen, B. L. Jensen, E. J. Montgomery, D. W. Feldman, P. G. O'Shea, and N. Moody, Theory of photoemission from cesium antimonide using an alpha-semiconductor model, *J. Appl. Phys.* **104**, 044907 (2008).

[16] K. L. Jensen, P. G. O'Shea, and D. W. Feldman, Emittance of a photocathode: Effects of temperature and field, *Phys. Rev. ST Accel. Beams* **13**, 080704 (2010).

[17] L. Cultrera, I. Bazarov, A. Bartnik, B. Dunham, S. Karkare, R. Merluzzi, and M. Nichols, Thermal emittance and response time of a cesium antimonide photocathode, *Appl. Phys. Lett.* **99**, 152110 (2011).

[18] C. Parzyck, C. Pennington, W. DeBenedetti, J. Balajka, E. Echeverria, H. Paik, L. Moreschini, B. Faeth, C. Hu, J. Nangoi, *et al.*, Atomically smooth films of cssb: A chemically robust visible light photocathode, *APL Mater.* **11**, 101125 (2023).

[19] P. P. Owusu, J. Mama, T. Idso, A. Ullattuparambil, M. M. Rizi, J. Anawalt, and S. Karkare, Characterization of cs3sb photocathodes at cryogenic temperatures, *Appl. Phys. Lett.* **127**, 172101 (2025).

[20] K. L. Jensen, Y. Lau, D. W. Feldman, and P. O'Shea, Electron emission contributions to dark current and its relation to microscopic field enhancement and heating in accelerator structures, *Phys. Rev. ST Accel. Beams* **11**, 081001 (2008).

[21] J. K. Nangoi, S. Karkare, R. Sundararaman, H. A. Padmore, and T. A. Arias, Importance of bulk excitations and coherent electron-photon-phonon scattering in photoemission from pbte (111): Ab initio theory with experimental comparisons, *Phys. Rev. B* **104**, 115132 (2021).

[22] E. R. Antoniuk, P. Schindler, W. A. Schroeder, B. Dunham, P. Pianetta, T. Vecchione, and E. J. Reed, Novel ultrabright and air-stable photocathodes discovered from machine learning and density functional theory driven screening, *Adv. Mater.* **33**, 2104081 (2021).

[23] P. Schindler, E. R. Antoniuk, G. Cheon, Y. Zhu, and E. J. Reed, Discovery of stable surfaces with extreme work functions by high-throughput density functional theory and machine learning, *Adv. Funct. Mater.* **34**, 2401764 (2024).

[24] V. Chang, T. Noakes, and N. Harrison, Work function and quantum efficiency study of metal oxide thin films on ag (100), *Phys. Rev. B* **97**, 155436 (2018).

[25] I. Napier, V. Chang, T. Noakes, and N. Harrison, From electronic structure to design principles for photocathodes: Cu-ba alloys, *Phys. Rev. Appl.* **11**, 064061 (2019).

[26] C. Cocchi, S. Mistry, M. Schmeißer, J. Kühn, and T. Kamps, First-principles many-body study of the electronic and optical properties of csk<sub>2</sub>sb, a semiconducting material for ultra-bright electron sources, *J. Phys. Con-*

dens. Matter. **31**, 014002 (2019).

[27] R. Amador, H.-D. Saßnick, and C. Cocchi, Electronic structure and optical properties of na2ksb and nak2sb from first-principles many-body theory, J. Phys. Condens. Matter. **33**, 365502 (2021).

[28] C. Cocchi and H.-D. Saßnick, Ab initio quantum-mechanical predictions of semiconducting photocathode materials, Micromachines **12**, 1002 (2021).

[29] R. Schier and C. Cocchi, Electronic and optical excitations of k-sb and na-sb crystals, Phys. Rev. Materials **9**, 053804 (2025).

[30] C. Xu, R. Schier, and C. Cocchi, Electronic and optical properties of computationally predicted na-k-sb crystals, Electron. Struct. **7**, 015001 (2025).

[31] P. Hohenberg and W. Kohn, Inhomogeneous electron gas, Phys. Rev. **136**, B864 (1964).

[32] G. Onida, L. Reining, and A. Rubio, Electronic excitations: density-functional versus many-body green's function approaches, Rev. Mod. Phys. **74**, 601 (2002).

[33] W. Kohn and L. J. Sham, Self-consistent equations including exchange and correlation effects, Phys. Rev. **140**, A1133 (1965).

[34] H.-D. Saßnick and C. Cocchi, Electronic structure of cesium-based photocathode materials from density functional theory: Performance of pbe, scan, and hse06 functionals, Electron. Struct. **3**, 027001 (2021).

[35] J. Sun, A. Ruzsinszky, and J. P. Perdew, Strongly constrained and appropriately normed semilocal density functional, Phys. Rev. Lett. **115**, 036402 (2015).

[36] R. Schier, H.-D. Saßnick, and C. Cocchi, Stability and electronic properties of csk 2 sb surface facets, Phys. Rev. Materials **6**, 125001 (2022).

[37] H.-D. Saßnick and C. Cocchi, Automated analysis of surface facets: the example of cesium telluride, npj Comput. Mater. **10**, 38 (2024).

[38] R. Schier, D. Guo, H.-D. Saßnick, and C. Cocchi, Stability and electronic properties of k-sb and na-sb binary crystals from high-throughput ab initio calculations, Adv. Theory Simul. **7**, 2400680 (2024).

[39] L. Hedin, New method for calculating the one-particle green's function with application to the electron-gas problem, Phys. Rev. **139**, A796 (1965).

[40] L. Reining, The gw approximation: content, successes and limitations, Wiley Interdiscip. Rev. Comput. Mol. Sci. **8**, e1344 (2018).

[41] E. E. Salpeter and H. A. Bethe, A relativistic equation for bound-state problems, Phys. Rev. **84**, 1232 (1951).

[42] J. Dube, J. Kühn, C. Wang, S. Mistry, G. Klemz, A. Galdi, and T. Kamps, Triple evaporation growth and photoemission characterization of bialkali antimonide photocathodes, J. Appl. Phys. **138**, 045704 (2025).

[43] C. Wang, J. Dube, A. Galdi, T. Kamps, and J. Kühn, Triple evaporation growth of sodium-potassium-antimonide thin films as photoemission source for electron accelerators, J. Phys. D DOI: 10.1088/1361-6463/ae4246 (2026).

[44] M. A. Schmeïßer, S. Mistry, H. Kirschner, S. Schubert, A. Jankowiak, T. Kamps, and J. Kühn, Towards the operation of cs-k-sb photocathodes in superconducting rf photoinjectors, Phys. Rev. ST Accel. Beams **21**, 113401 (2018).

[45] C. Cocchi, S. Mistry, M. Schmeïßer, R. Amador, J. Kühn, and T. Kamps, Electronic structure and core electron fingerprints of caesium-based multi-alkali antimonides for ultra-bright electron sources, Sci. Rep. **9**, 18276 (2019).

[46] H. Kirschner, A. Jankowiak, T. Kamps, J. Kühn, M. Schmeïßer, *et al.*, Measuring the spectral response of cs-k-sb photocathodes for berlinpro, in *8th Int. Particle Accelerator Conf. (IPAC'17), Copenhagen, Denmark* (2017).

[47] C. Vorwerk, B. Aurich, C. Cocchi, and C. Draxl, Bethe-salpeter equation for absorption and scattering spectroscopy: implementation in the exciting code, Electron. Struct. **1**, 037001 (2019).

[48] P. Gupta, L. Cultrera, and I. Bazarov, Monte carlo simulations of electron photoemission from cesium antimonide, J. Appl. Phys. **121**, 215702 (2017).

[49] D. H. Dowell and J. F. Schmerge, Quantum efficiency and thermal emittance of metal photocathodes, Phys. Rev. ST Accel. Beams **12**, 074201 (2009).

[50] S. Karkare, D. Dimitrov, W. Schaff, L. Cultrera, A. Bartnik, X. Liu, E. Sawyer, T. Esposito, and I. Bazarov, Monte carlo charge transport and photoemission from negative electron affinity gaas photocathodes, J. Appl. Phys. **113**, 104904 (2013).

[51] O. Chubenko, S. Karkare, D. A. Dimitrov, J. K. Bae, L. Cultrera, I. Bazarov, and A. Afanasev, Monte carlo modeling of spin-polarized photoemission from p-doped bulk gaas, J. Appl. Phys. **130**, 063101 (2021).

[52] W. E. Spicer, Photoemission and related properties of the alkali-antimonides, J. Appl. Phys. **31**, 2077 (1960).

[53] P. Musumeci, J. G. Navarro, J. Rosenzweig, L. Cultrera, I. Bazarov, J. Maxson, S. Karkare, and H. Padmore, Advances in bright electron sources, Nucl. Instrum. Methods Phys. Res. A **907**, 209 (2018).

[54] S. K. Mohanty, M. Krasilnikov, A. Oppelt, F. Stephan, D. Sertore, L. Monaco, C. Pagani, and W. Hillert, Development and characterization of multi-alkali antimonide photocathodes for high-brightness rf photoinjectors, Micromachines **14**, 1182 (2023).

[55] B. Erjavec, Activation of the na2ksb photocathode with cs and o2 at lowered temperatures, Appl. Surf. Sci. **103**, 343 (1996).

[56] J. Santana-Andreo, H.-D. Saßnick, and C. Cocchi, Thermodynamic stability and vibrational properties of multi-alkali antimonides, J. Phys. Mater. **7**, 035004 (2024).

[57] T. Yue, P. Sui, Y. Zhao, J. Ni, S. Meng, and Z. Dai, Theoretical prediction of mechanics, transport, and thermoelectric properties of full heusler compounds na 2 ksb and x 2 cssb (x = k, rb), Phys. Rev. B **105**, 184304 (2022).

[58] L. Cultrera, C. Gulliford, A. Bartnik, H. Lee, and I. Bazarov, Ultra low emittance electron beams from multi-alkali antimonide photocathode operated with infrared light, Appl. Phys. Lett. **108**, 134105 (2016).

[59] A. Galdi, J. Balajka, W. J. DeBenedetti, L. Cultrera, I. V. Bazarov, M. A. Hines, and J. M. Maxson, Reduction of surface roughness emittance of cs3sb photocathodes grown via codeposition on single crystal substrates, Appl. Phys. Lett. **118**, 244101 (2021).

[60] C. T. Parzyck, A. Galdi, J. K. Nangoi, W. J. I. DeBenedetti, J. Balajka, B. D. Faeth, H. Paik, C. Hu, T. A. Arias, M. A. Hines, D. G. Schlom, K. M. Shen, and J. M. Maxson, Single-crystal alkali antimonide photocathodes: High efficiency in the ultrathin limit, Phys. Rev. Lett. **128**, 114801 (2022).

[61] M. A. H. Schmeïßer, *Photocathodes for high brightness, high average current photoelectron injectors* (Humboldt Universität zu Berlin, Germany, 2019).

- [62] F. Wooten, J. Hernandez, and W. Spicer, Photoemission and electron scattering in cs<sub>3</sub>bi and cs<sub>3</sub>sb, *J. Appl. Phys.* **44**, 1112 (1973).
- [63] A. Kachwala, P. Saha, P. Bhattacharyya, E. Montgomery, O. Chubenko, and S. Karkare, Demonstration of thermal limit mean transverse energy from cesium antimonide photocathodes, *Appl. Phys. Lett.* **123**, 044106 (2023).
- [64] C. Vorwerk, C. Cocchi, and C. Draxl, Layeroptics: Microscopic modeling of optical coefficients in layered materials, *Comput. Phys. Commun.* **201**, 119 (2016).
- [65] C. Cocchi and C. Draxl, Bound excitons and many-body effects in x-ray absorption spectra of azobenzene-functionalized self-assembled monolayers, *Phys. Rev. B* **92**, 205105 (2015).
- [66] C. Cocchi, H. Zschiesche, D. Nabok, A. Mogilatenko, M. Albrecht, Z. Galazka, H. Kirmse, C. Draxl, and C. T. Koch, Atomic signatures of local environment from core-level spectroscopy in  $\beta$ -ga 2 o 3, *Phys. Rev. B* **94**, 075147 (2016).
- [67] C. Cocchi, T. Breuer, G. Witte, and C. Draxl, Polarized absorbance and davydov splitting in bulk and thin-film pentacene polymorphs, *Phys. Chem. Chem. Phys.* **20**, 29724 (2018).